Computational Particle Mechanics manuscript No.
(will be inserted by the editor)

Discrete element modelling of concrete under high-stress level: influence of saturation ratio

Hicham Benniou[1] · **Abdallah Accary**[1] · **Yann Malecot**[1] · **Matthieu Briffaut**[1] ·
Laurent Daudeville[1*]

Received: date / Accepted: date

Abstract The discrete element model proposed in this paper addresses the macroscopic behavior of concrete taking into account the presence of free water in pores, thanks to a new interaction law between spherical discrete elements (DE). When concrete structures are subjected to a severe loading, e.g. an impact, material exhibits high triaxial compressive stresses which are highly influenced by the saturation ratio. In this new constitutive model, cracking and compaction are modeled at the interaction level between DEs and free water effects are taken into account by introducing a dependency between the water saturation ratio and the inelastic deformation due to the pore closure. The present numerical model has been implemented within the YADE (Yet Another Dynamic Engine) code in order to deal with extreme loading situations leading to stress states characterized by a high mean stress level.

Keywords DEM · Discrete element model · Concrete · Saturation ratio · Confined compression

1 Introduction

When a concrete structure is subjected to an intense loading, e.g. an impact, the material in the vicinity of the loading zone undergoes high levels of stress leading to irreversible compaction, whereas farther from this location, compression with a moderate triaxial stress level occurs [13], [7], [34].

The quasi-static constitutive behavior of an ordinary concrete was extensively studied at 3SR laboratory thanks to triaxial compression tests performed with a large capacity press named Giga [37]. Under high confinement (some hundreds MPa), the water saturation of concrete plays a major role [38]. On the one hand, the hydrostatic behavior of wet or saturated concrete clearly becomes stiffer than that of dry concrete. On the other hand, the shear strength of wet or saturated concrete seems limited to a maximum value independent on the confining pressure, while the shear strength of dry concrete increases almost linearly with confining pressure. The limit shear strength value is directly correlated with the water saturation ratio of concrete [38]. It is also worth noting that all these tests are performed under quasi-static undrained conditions similarly to impact condition; as the water has not enough time to migrate during impact.

Because protective concrete structures are generally massive, they may have a core partially or fully water saturated whereas the skin is dry. Accounting the effect of water saturation ratio is then particularly relevant for massive concrete structures submitted to very high stress level.

The PRM coupled model [25], [40] is a finite element (FE) model that uses the effective stress concept developed by Mariotti et al. [20] for wet geomaterials under high stress level. Thus, such a model takes into account the saturation ratio, but finite element models are not well adapted for large discontinuity and perforation simulations. The discrete element method (DEM) has several advantages. It can easily represent discontinuities caused by cracking or fragmentation and reproduce the macroscopic behavior of concrete. Several DE models were developed to reproduce the behavior of granular and cohesive materials [4], [5], [6], [9], [14], [24], [31], [33], [35], but none of them accounts for the effects of saturation ratio.

This paper presents a new local constitutive behavior for discrete element modelling of concrete structures that attempts to take into account the influence of free water into the porous concrete material under very high quasi-static stress level. The proposed model is based on the use

---

[*] Corresponding author: Laurent Daudeville
E-mail: laurent.daudeville@univ-grenoble-alpes.fr
[1] Univ. Grenoble Alpes, CNRS, Grenoble INP, 3SR, 38000 Grenoble, France

of spherical DEs, it was developed for concrete that is a cohesive material. Thus, contrarily to models developed for granular materials [4], cohesive interactions are considered between elements that are not in contact. As long as the material is cohesive, the proposed approach is similar to lattice models [30], [17], [44]. Once fracture and fragmentation occurs, contact interactions may be created and easily handled with spherical DEs. The DE model is implanted is the open source code YADE [15] with the aim of modelling the behavior of concrete at the macroscopic scale to deal with impact problems on structures [43], [42]. Thus the internal structure of concrete (aggregates, cement paste, pores) is not described like in [16], [21] and [35]. In this study, the three dimensional DEM constitutive model implemented in YADE will be described. The model calibration and validation is based on triaxial compression tests performed with the large capacity press Giga of 3SR laboratory at the university Grenoble Alpes. Numerical simulations of tests performed on ordinary concrete samples at different saturation ratios including triaxial and oedometric tests will be discussed.

2 Discrete element background

The DEs are rigid spheres of different radii. Each of them has a mass and a rotational inertia. Note that DEs do not represent aggregates, interaction laws between DEs are chosen to represent the macroscopic behavior of concrete as well as discontinuities (cracks) that may appear in the medium. Cohesive interactions are spring-like connections in extension, shear and rotation. The interaction force F represents the action between two elements a and b is given in eq.(1). The interaction stiffness K and displacement U are decomposed to K_n, K_s and U_n, U_s acting in the normal and shear direction respectively.

$$F = KU \tag{1}$$

Using the constitutive model of each interaction, the numerical model solves the equation of motion of the spheres assembly. The new displacement, velocity and acceleration for each discrete element are calculated by solving the dynamic equilibrium equations based on an explicit time integration scheme conditionally stable. The condition of stability applied for motion equations is inspired from [4] and [27].

3 Constitutive model description

At macroscopic scale, the concrete can be considered as a homogeneous isotropic material. Under confined compression and increasing mean stress levels, concrete first follows a linear behavior, and then its tangent stiffness decreases due to the damage of cement matrix, which leads to porosity closure. During the porosity closure, the stiffness of the material increases and tends to the elastic stiffness of the fully consolidated material [19]. This behavior at the macroscopic scale can be reproduced through simple interaction laws between the discrete elements. Shiu et al. [32] developed an interaction law featuring an elastic quasi-brittle behavior in tension, and a three linear behavior in compression, but this model does not take into account the effect of the concrete saturation ratio. In this new model, the effect of free water is taken into account by introducing a dependency between water saturation ratio and inelastic deformations due to pore closure. The porosity closure is defined as a local variable at the interaction level using the decrease of the distance between DEs. A maximum shear stress criterion is also introduced to take into account the correlation between limit shear strength and saturation ratio. The proposed model is calibrated by means of test results performed on a reference ordinary concrete named R30A7. Gabet et al. [12], Vu et al. [39] and Piotrowska et al. [22], studied the triaxial behavior of dry, wet or fully saturated R30A7 concrete under a confinement stress up to 600 MPa. Experimental results obtained previously emphasized on the fact that the presence of free water in pores has an effect only when the free porosity (not occupied with water) is closed. According to our assumptions, if the boundary allows the water outflow, then the effect of water vanishes and the constitutive behavior of concrete will be that of dry concrete. Note that differed phenomena due to water migration are not taken into account in the model since, due to the low loading time, no water migration is assumed.

3.1 Interaction laws

In this model, interactions between DE neighbors that are not in contact are allowed by introducing an interaction radius coefficient ($I_r \geq 1$). Two types of interactions are defined: initial links and residual contacts. The value of I_r,which concerns only initial links, influences directly the number of interactions per sphere at the beginning of the calculation (eq.(2)). Rousseau et al. [28] showed that in order to achieve a realistic isotropic elastic behavior of concrete, this number should be around 12. The interaction radius coefficient I_r will be adjusted accordingly. As calculation is proceeded and due to external loading, changes in DEs arrangement occur and new contact interactions may be created while others vanish.

3.1.1 Cohesive interactions

Cohesive interactions are created between DEs within the same range at the beginning of the simulation. For instance, a link is created between elements a, and b of radius R_a and R_b respectively if:

$$I_r(R_a + R_b) \geq D^0_{ab} \tag{2}$$

Where D^0_{ab} is the initial distance between the centroids of elements a and b. D^0_{ab} is also the reference distance used later to convert displacement to dimensionless strain. If ${C^0}_a$ and ${C^0}_b$ are initial centroids position of elements a and b respectively, then:

$$D^0_{ab} = |{C^0}_a - {C^0}_b| \tag{3}$$

Tensile stress appears when the current distance between elements a and b: $D_{ab} = |C_a - C_b|$ is larger than the initial distance D^0_{ab} because the interaction is cohesive.

3.1.2 Contact interaction

Contact interactions can be created between DEs after the beginning of the simulation, either when a cohesive *Link* interaction is broken or when two DEs that were not in interaction are in contact $(R_a + R_b) \geq D^0_{ab}$.

3.2 Elastic interaction law

Interaction force F can be decomposed in a normal force F_n and a shear force F_s :

$$F_n = K_n U_n \tag{4}$$

$$F_s = K_s U_s \tag{5}$$

U_n and U_s are respectively normal and shear displacements. K_n and K_s are respectively normal and shear stiffnesses, both expressed using E an equivalent Young modulus and G an equivalent shear modulus for the link:

$$K_n = \frac{EA_{eq}}{D^0_{ab}} \tag{6}$$

$$K_s = \frac{GA_{eq}}{D^0_{ab}} \tag{7}$$

The macroscopic elastic properties, here Young modulus E (GPa) and shear modulus G (GPa), are thus considered to be an input parameters. A_{eq} is the interaction cross-section, and is defined as follows:

$$A_{eq} = \pi \times min(R_a, R_b)^2 \tag{8}$$

Thus, the forces could be defined from equivalent stresses as follows:

$$F_n = \sigma_n A_{eq} \tag{9}$$

$$F_s = \sigma_s A_{eq} \tag{10}$$

with,

$$\sigma_n = E\varepsilon_n \tag{11}$$

$$\sigma_s = G\varepsilon_s \tag{12}$$

where ε_n and ε_s are the equivalent normal and shear strain respectively

$$\varepsilon = \begin{bmatrix} \varepsilon_n \\ \varepsilon_s \end{bmatrix} \tag{13}$$

A fictitious interaction point P_c is defined at a mid-distance from the two elements and a vector **n** which is the normal to the contact plane that passes through P_c (always perpendicular to the contact plane). U_n is aligned with **n**. The shear displacement U_s must be expressed in the global coordinates while satisfying the condition $U_s \perp \mathbf{n}$. This is due to the lack of an interaction-local coordinate system. Indeed, each spherical contact only defines the contact normal and the contact plane (Figure 1).

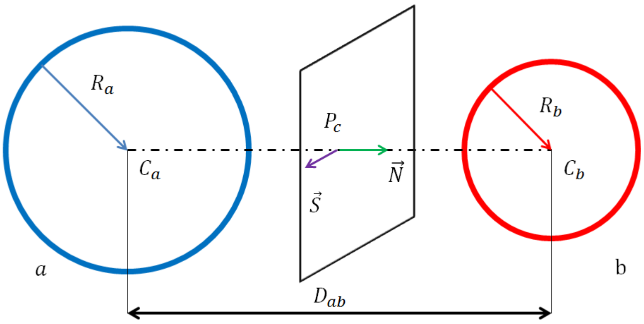

Fig. 1 Interaction between two elements. Force and displacement components

As large strains are expected, logarithmic strains, also equivalent to the sum of incremental strains are used (eq. (14)). The strain tends to $-\infty$ if two centers of spheres approach from one another, which avoid them to penetrate through each other.

$$\varepsilon = \begin{bmatrix} \varepsilon_n \\ \varepsilon_s \end{bmatrix} = \begin{bmatrix} \log(\frac{U_n}{D^0}) \\ \sum \frac{\delta U_s}{D^0} \end{bmatrix} \tag{14}$$

For torque computation, the following equations are used:

$$M_b = \sum \delta\theta_b K_b \tag{15}$$

$$M_t = \sum \delta\theta_t K_t \tag{16}$$

$\delta\theta_b$ and $\delta\theta_t$ are the incremental bending and twisting rotation angle respectively. K_b and K_t bending and twisting stiffnesses that are estimated by considering that a circular beam, with a section A_{eq}, connects the two centroids of spheres a and b (eq. (8)). To limit the torque, two dimensionless parameters $\alpha_b, \alpha_t \in [0,1]$ are used such that:

$$K_b = \alpha_b\, K_s\, A_{eq} \tag{17}$$

$$K_t = \alpha_t\, K_s\, A_{eq} \tag{18}$$

3.3 Nonlinear interaction behavior

As shown in equations (eq. (11) and eq. (12)), σ_n and σ_s are related to ε_n and ε_s respectively. This relation between stress and strain at the link scale characterizes the interaction behavior in both tension and compression.

3.3.1 Tension

Beyond the elastic limit ε_0, a damage behavior in tension is applied. Normal stress σ_n is formulated as follows:

$$\sigma_n = [1-\omega(\kappa)\mathrm{H}(\kappa-\varepsilon_0)]E\varepsilon_n \tag{19}$$

κ is the maximum normal strain ($\kappa = max(\varepsilon_n)$), $\omega(\kappa)$ is the damage evolution function, and H is a Heaviside function that deactivates damage effect if $\kappa < \varepsilon_0$. The damage evolution function ω is described as follows:

$$\omega(\kappa) = \frac{1-\frac{\varepsilon_0}{\kappa}}{1-\frac{\varepsilon_0}{\varepsilon_f}} \quad \text{if } \varepsilon_0 \leq \kappa \leq \varepsilon_f \tag{20}$$

ε_f is the maximum strain corresponding to the maximum damage ($\omega = 1$ when $\varepsilon_n = \varepsilon_f$). Beyond this point, the link between the spheres is deleted and a new contact interaction is created only if these two spheres touch again. Figure 2 shows the evolution of the damage and the tensile stress in the normal direction.

3.3.2 Compression

The interaction model between DEs is a beam-like model whose constitutive behavior is phenomenological. It means that the local constitutive behavior is inspired from observations at the macro scale, including compaction (pore closure). Thus, under normal compression the stiffness varies between the initial elastic stiffness K_n (directly linked to the Young modulus) and the consolidated material stiffness k_h x k_n (k_h ¿1 is an non-dimensional parameter). k_p and k_h values are calibrated by means of simulation of confined compression tests. Thus, in compression the behavior phases are defined as follow (see Fig.3):

Phase [A B]: linear zone of the link, characterized by the initial elastic stiffness of the material. ε_{el} is the elastic limit strain in compression.

$$\sigma_n = E\varepsilon_n \quad \text{for} \quad \varepsilon_n < \varepsilon_{el} \tag{21}$$

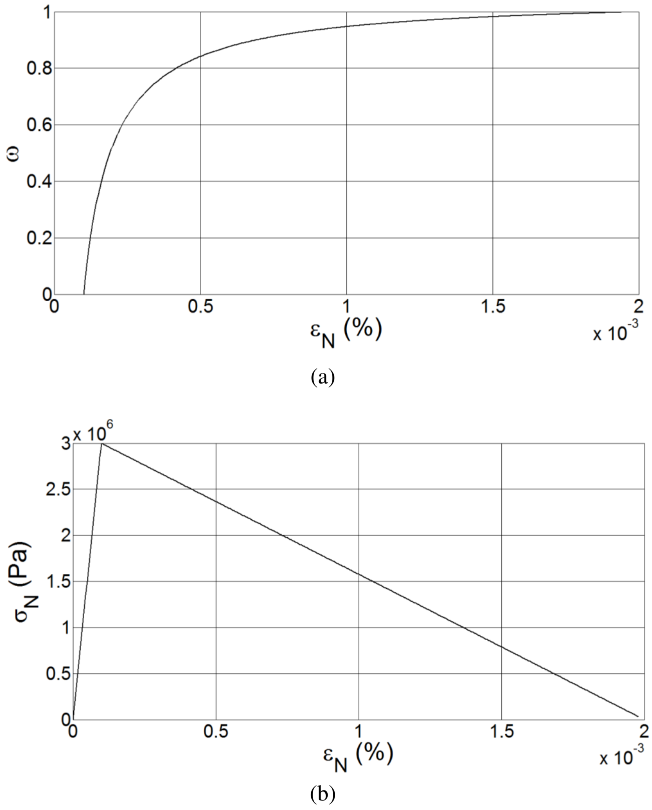

Fig. 2 a Damage evolution ω vs. normal strain ε_n in a cohesive interaction. b Corresponding tensile stress σ_n vs. ε_n

Phase [B C]: compaction zone, the elastic stiffness of the link varies linearly between the initial elastic stiffness and the consolidated material stiffness. Let us note that at this point porosity is inherently defined at the link scale since ε_{pl} is the maximum deformation corresponding to a complete porosity closure. k_p is the strain hardening modulus introduced as:

$$\sigma_n = \frac{E}{k_p}(\varepsilon_n - \varepsilon_{el}) + \sigma_{el_{max}} \quad \text{for} \quad \varepsilon_{el} < \varepsilon_n < \varepsilon_{pl} \tag{22}$$

Phase [C D]: consolidated material zone. Beyond this point, the link is fully compacted and the response is incrementally elastic again as described in (eq. 23). Figure 3 also shows the cyclic behavior of a link in the normal direction (interaction level).

$$\sigma_n = Ek_h(\varepsilon_n - \varepsilon_{pl}) + \sigma_{pl_{max}} \quad \text{for} \quad \varepsilon_{pl} < \varepsilon_n \tag{23}$$

3.3.3 Shear

As explained in (sec. 3.2) the elastic shear stress σ_s can be defined as shown in (eq. (12)). The shear response is then limited by the maximum shear stress surface (Figure 4). The shear stress criterion $\sigma_{s_{max}}$ (see eq. (24)) is characterized by

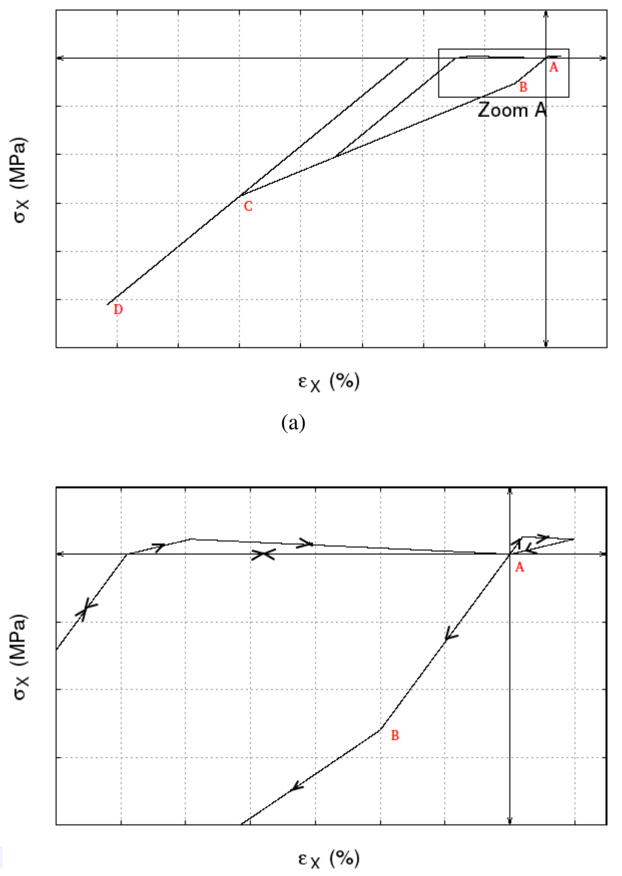

(a)

(b)

Fig. 3 Cyclic loading of a single cohesive link. a In the normal direction. b Zoom of A region

the initial shear cohesion of the link C_0, the friction angle Φ, and a maximum shear stress (1+λ)C_0 allowing sliding (plastic slip) between spheres.

$$\sigma_{s_{max}} = (1-\omega)C_0 + \frac{\lambda C_0 \sigma_n tan(\Phi)}{\sigma_n tan(\Phi) + (\lambda + 1 - \omega)F_t} \tag{24}$$

ω is the damage function, F_t the undamaged tensile strength (F_t=Eε_0) and λ a dimensionless parameter that allows controlling the maximum shear stress asymptote.

3.4 Effect of saturation ratio (Sr) on the compressive behavior

The effect of free water on concrete mechanical behavior has been widely studied under high or moderate strain rates [29], [45], [41], [36]. Due to a lack of experimental data, there is no available discrete element model dealing with free water influence on the mechanical behaviour of concrete under high stress level. The proposed model is the first attempt aiming at filling this gap.

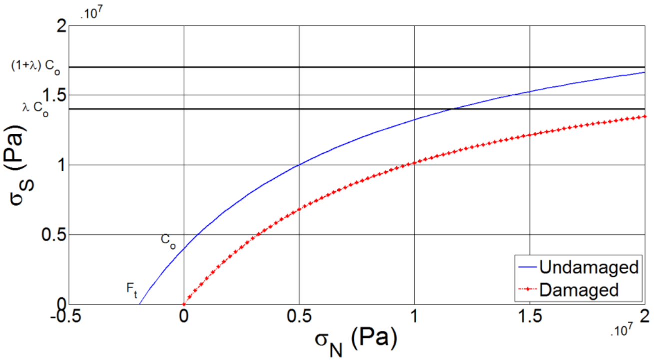

Fig. 4 Maximum shear stress surface versus uniaxial stress at the link scale

Saturation ratio is introduced as a local variable at the interaction level between spheres and its evolution is related to the porosity closure during the compaction phase described by (eq. (22)). In this paper, an initial homogeneous, saturation ratio distribution is assumed in the sample however the structural heterogeneity, or a heterogeneity based on the DE size or position, could easily be taken into account. Note that, the effect of saturation ratio is taken into account for compressive stress only. As it was explained in (sec. 3.3.2), for a dry link ($S_r = 0\%$), the consolidation point is defined accordingly to normal strain, and it corresponds to a complete porosity closure ($\varepsilon_n = \varepsilon_{pl}$). Then, the general idea of the model is to assure that a smaller deformation is needed to close a partially saturated porosity as a fraction of it is already occupied by water. The higher the saturation ratio is, the earlier the consolidation point will be reached and the effect of water will begin to appear on the mechanical behavior. Thus, the new consolidation point $\varepsilon_{n,plC}$ is defined as a linear function of S_r which is the saturation ratio of the link:

$$\varepsilon_{n,plC} = \varepsilon_{el} + (\varepsilon_{pl} - \varepsilon_{el})(1 - S_r) \tag{25}$$

From equation (eq. (25)), it is clear that if the link is dry ($S_r = 0$), $\varepsilon_{n,plC}$ is equal to ε_{pl} while if the link is completely saturated ($S_r = 1$) and then $\varepsilon_{n,plC}$ is equal to ε_{el}. A kind of effective stress concept is then introduced to take into account the water contribution in the total stress at the link scale using Biot coefficient assumed to be, at the first order, equal to the porosity φ. The variation of the porosity is defined accordingly to the volumetric strain ε_v which is defined from the normal strain of the unidimensional link as $\varepsilon_v = 3\varepsilon_n$ and to φ_i which is the initial porosity of the sample. Thus:

$$\sigma_{n_{total}} = \sigma_n + 3\varphi\sigma_{n_{water}} \tag{26}$$

One can remark from (eq. (26)) that the water contribution will increase with the porosity and with the saturation ratio. Note that a $Mie - Gruneisen$ like equation of state is used to take into account water compressibility and to compute the water contribution in the total stress [8] (eq. (27)):

$$\sigma_{water} = \frac{\rho_0 C_{w0}^2(\varepsilon_v - \varepsilon_{v,ps})}{(1 - s(\varepsilon_v - \varepsilon_{v,ps}))^2}[1 - \frac{\Gamma_0(\varepsilon_v - \varepsilon_{v,ps})}{2}] \quad (27)$$

Where $\varepsilon_{v,ps}$ is the volumetric strain at the consolidation point ($\varepsilon_{v,ps} = 3\varepsilon_{n,plc}$), C_{w0} is the sound-wave velocity, ρ_0 is the mass density, s and Γ_0 are two Mie-Gruneisen coefficients. The interstitial water pore pressure was recently investigated and measured experimentally by [1] showing that it might reach several hundreds of megapascal under high confinement pressure. Figure 5 shows the normal compressive behavior of a dry link compared to that of a wet link ($S_r = 44\%$) and the corresponding water pressure. The consolidation point (CP) is reached earlier in the wet link hence the water contribution is added. In the dry link, reaching the consolidation point does not add any water contribution.

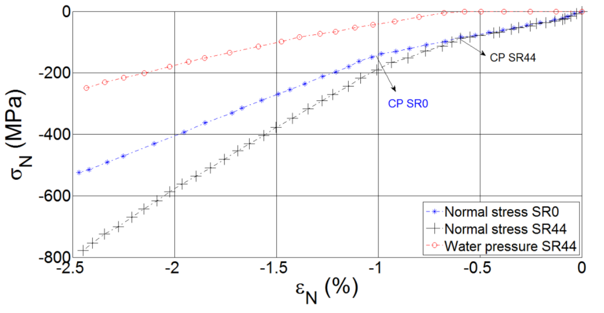

Fig. 5 Effect of the water contribution on the normal compressive stress-strain law at the link scale for $S_r = 44\%$ compare to $S_r = 0\%$

3.5 Effect of saturation ratio on the maximum shear stress

In order to control the plastic sliding threshold of interactions, a coefficient λ was introduced in eq. (24). This coefficient control the maximal limit shear strength of a link (λC_0) once the material is fully consolidated as observed experimentally by [38]. Two parameters λ_0 and λ_{100}, are calibrated for a dry and saturated links respectively and introduced to express λ as a linear function of the saturation ratio:

$$\lambda = (\lambda_0 - \lambda_{100})(1 - S_r) + \lambda_{100} \quad (28)$$

Thus, when $\lambda = \lambda_0$ then $\varepsilon_{n,plC} = \varepsilon_{pl}$ and when $\lambda = \lambda_{100}$ then $\varepsilon_{n,plC} = \varepsilon_{el}$. Figure 6 shows the dependency of the criterion on the saturation ratio. We can observe that the higher the saturation ratio is, the lower is the shear stress limit.

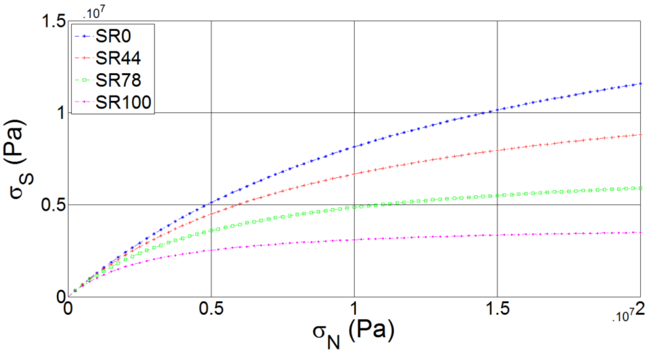

Fig. 6 Maximum shear stress surface for different saturation ratios ($S_r = 0\%$, $S_r = 44\%$, $S_r = 78\%$ and $S_r = 100\%$) at the link scale

4 Model calibration and validation

4.1 Numerical tests preparation and monitoring

The calibration is done by running simulations on sufficiently large numerical specimens to give continuum-like behavior. Samples, made of spheres, have to be isotropic to ensure a homogeneous interaction distribution in the sample and to prevent the forces from being in privileged directions [28], [10]. The isotropy of the numerical medium is verified by plotting the cumulative orientation distribution of interactions (Figure 7).

The histogram of the size distribution obtained for a specimen is shown in Figure 8(a). The size distribution goes from 2 to 4 mm and is homogeneously distributed between these extremum. The numerical compacity of the sample is about 0.6 and the interaction radius I_r is chosen in order to have an average of 12 interactions per element ($I_r = 1.5$). Figure 8(b) shows the numerical sample. It is a cuboid-shaped packing ($70mm \times 70mm \times 140mm$) of approximately 4000 spheres. It was checked that the shape of the numerical specimen does not affect the results since the stress state is homogeneous across the specimen.

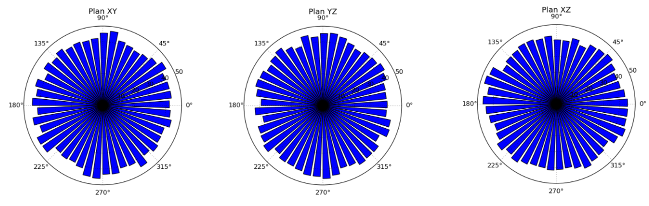

Fig. 7 Initial distribution of the interaction links' orientations in the numerical sample

Uniaxial and triaxial tests are then simulated in order to calibrate the model parameters. The calibration process, described in the next section, aims at identifying the model parameters values that allow reproducing the macroscopic behavior obtained in the tests performed on the R30A7 refer-

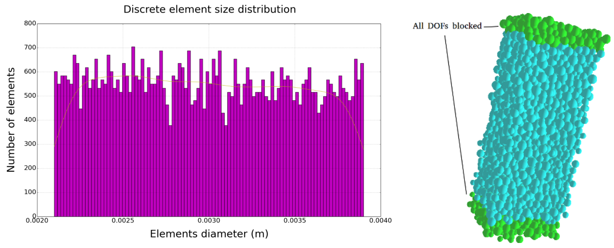

(a) (b)

Fig. 8 Size distribution of the sphere diameters in the numerical sample. a Histogram. b Numerical sample

ence concrete (unconfined compressive strength of 34 MPa, 7 cm slump, w/c = 0.64, 12% porosity accessible to water, see [11] for more details).

4.2 Model calibration and comparison with experiments

4.2.1 Uniaxial compression and tensile tests

Uniaxial tension or compression tests allow determining elastic parameters E, ν, initial cohesion C_0, limit elastic strain in tension ε_0 and the limit failure strain ε_f. The displacement is applied on boundary particles symmetrically on both ends of the specimen while restraining their other degrees of freedom. Average axial stress is obtained by averaging forces on both boundary particles divided by the specimen cross-section (assumed constant during the test). Figure 9 shows the numerical stress-strain curve in uniaxial compression, it is compared with a cyclic test result [23]. The stress-strain curve in tension is not available, only the tensile strength (3.2 MPa) could be obtained experimentally. Figure 10 shows a comparison between numerical and experimental failure patterns in the sample for uniaxial tension and compression tests respectively. In tension, a single crack appears; the stress state is homogeneous far from the ends of the specimen so its location depends on the statistical distribution of spheres into the sample. In compression, the ends are fixed then a typical cone failure pattern can be observed in the central part of the specimen. Benniou [2] has shown in his PhD that there is no mesh dependency for a moderate variation of DE sizes; this result was also shown in [26]. Note that Benniou [2] has also verified that uniaxial compresssion and tensile test results do not depend on the initial saturation ratio of concrete samples.

4.2.2 Triaxial compression tests at high level of confinement (600 MPa)

Tests at 600 MPa of confinement are used to calibrate parameters given in Table 2. It has been checked experimentally that the stress state during confined compression tests is homogeneous in the circular section specimens [37]. In a sake of simplicity, the DE specimen has a parallelepipedic shape with 6 contacts surfaces. This choice allows prescribing simple boundary conditions by means of six rigid walls; it has no influence since the obtained stress state is homogeneous. Triaxial calibration tests are run on dry ($S_r = 0\%$) and completely saturated ($S_r = 100\%$) numerical sample. These tests are conducted in two steps. The first phase is the hydrostatic compression, for which all the wall displacements are the same with a controlled velocity until the target confinement pressure P_c is reached $\sigma_x = \sigma_y = \sigma_z = \sigma_m = -P_c$. This step allows the calibration of non-linear parameters k_p, k_h, ε_{el} and ε_{pl}, (see Table 2, left part). The second phase is the deviatoric compression, for which the axial displacement is controlled on the top and bottom wall whereas all four other

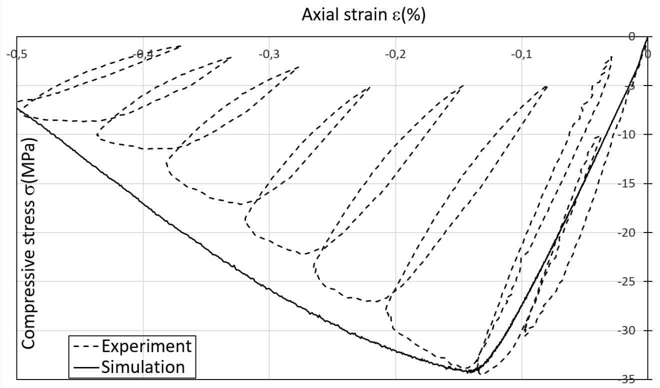

Fig. 9 Numerical stress-strain curve in uniaxial compression and comparison with experimental curve of a cyclic test [23]

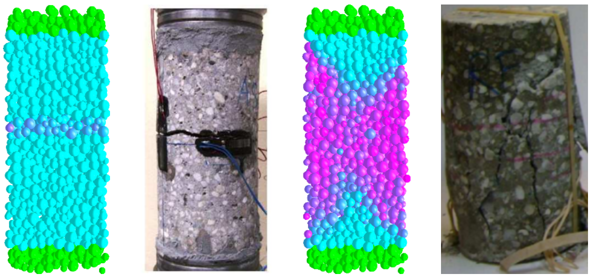

(a) (b) (c) (d)

Fig. 10 Comparison between numerical and experimental damage after uniaxial test: blue elements links are undamaged, red elements links are completely damaged. a,b Tension [11]; c,b Compression test [23]

Table 1 Model parameters calibration values from uniaxial tests

Parameters	Physical meaning	Values
E (GPa)	Young modulus	30
ν	Poisson ratio	0.2
ε_0	limit elastic strain in tension	$1e^{-4}$
ε_f	limit failure strain	$20\varepsilon_0$
Φ_c (radians)	contact friction angle	0.8
C_0 (MPa)	shear cohesion	4

walls are monitored by their normal stress so that constant $\sigma_y = \sigma_z = -P_c$. This step allows the calibration of the two last parameters λ_{100} and λ_0, (see Table 2).

Table 2 Model parameters calibration values from triaxial compression tests at 600 MPa

Parameters	Physical meaning	Values
k_p	strain hardening modulus	2
k_h	consolidated material parameter	1
ε_{el}	limit elastic strain in compression	$20\varepsilon_0$
ε_{pl}	maximum compaction strain	$200\varepsilon_0$
λ_{100}	saturated sliding threshold coefficient	1
λ_0	dry sliding threshold coefficient	5

Figures 11 and 12 display the results of experimental tests carried out by [18] and of numerical simulations obtained for an hydrostatic and deviatoric compression phase respectively for ($S_r = 0\%$) and ($S_r = 100\%$). Numerical simulations show a good agreement with experimental tests and the capability of the model to reproduce results at the macroscopic scale. The effect of saturation ratio is pronounced for hydrostatic phase as shown in Figure 11, a relative difference of about 25% between the volumetric strains of dry and saturated samples at a mean stress of 600 MPa is observed. For deviatoric phase, the saturation ratio notably affects the shear limit as shown in Figure 12. At 600 MPa of confinement pressure, the shear resistance drops from 800 MPa for a dry sample to 250 MP for a saturated sample which is only due to the presence of free water in the saturated sample. Note on Figure 12 that the comparison between the experimental and numerical results is not perfect for dry concrete and an axial strain greater than 8%; it is a minor drawback of the DE model that the authors did not try to fix because the maximum deviatoric stress varies slightly for different tests performed on dry concrete [12].

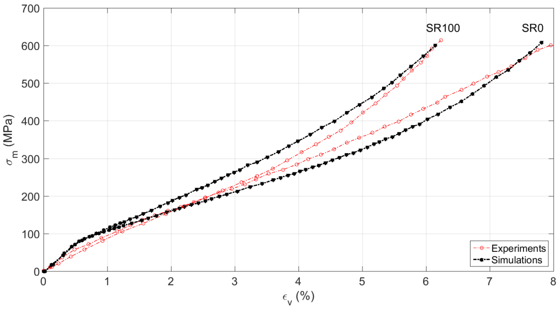

Fig. 11 Hydrostatic compression test; mean stress vs. volumetric strain: comparison between experiment and modelling for $S_r = 0\%$ and $S_r = 100\%$

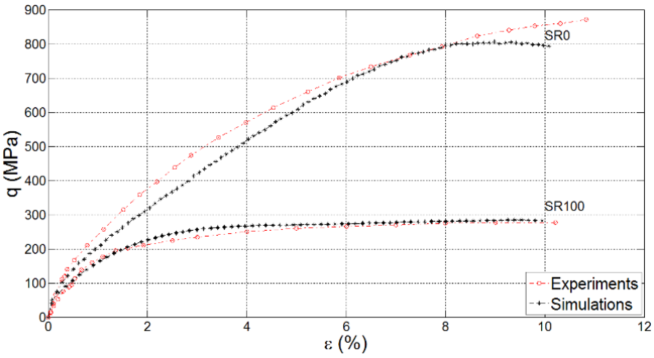

Fig. 12 Deviatoric phase of triaxial test at P_c=600 MPa, deviatoric stress vs. axial strain: comparison between experiment and modelling for $S_r = 0\%$ and $S_r = 100\%$

4.3 Model validation

4.3.1 Hydrostatic tests at different saturation ratio (600 MPa)

Figure 13 presents simulation results for hydrostatic compression tests at different saturation ratios. This figure shows that beyond the consolidation point, the mean stress increases and the volumetric strain decreases for higher saturation ratios.

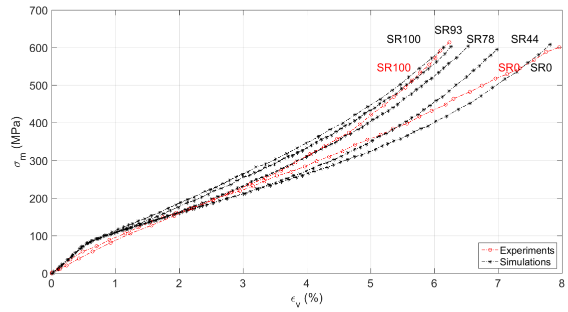

Fig. 13 Simulation of hydrostatic compression test; mean stress vs. volumetric strain for different saturation ratios ($S_r = 0\%$, $S_r = 44\%$, $S_r = 78\%$, $S_r = 93\%$ and $S_r = 100\%$)

4.3.2 Triaxial tests at moderate confining pressure (at 100 and 200 MPa)

Figure 14 shows simulation results of the deviatoric phase of triaxial tests at 100 MPa and 200 MPa compared to experimental results obtained by [18] for different saturation ratios. Triaxial tests at moderate confining pressures are difficult to simulate because these mean stress levels correspond to the transition from brittle to ductile behavior, which means, to have in the same time a significant effect of both damage and plasticity. However, Figure 14 shows that the simulation results are in good agreement with the experimental ones.

From the one hand, Fig. 12 and 14 indicate that the deviatoric behavior of dry concrete is highly influenced by the confining pressure since as the confining pressure increases from 100 to 600 MPa the deviatoric stress increases from 250 to 800 MPa. From the other hand, for a given confinement pressure and for intermediate saturation ratios (Fig. 14(a) and 14(b)), the peak deviatoric stress lies between the dried and saturated limit cases and seems to be associated directly to the saturation ratio. Thus the limit stress decreases when the saturation ratio increases. Fig. 14(b)) shows non-satisfying agreements for the 200 MPa confinement triaxial tests with initial saturation ratio Sr equal to 78% and 100%; all other results are very good. The authors explain these results by a possible overestimation of S_r [38], the two samples might have slightly dried just before the tests.

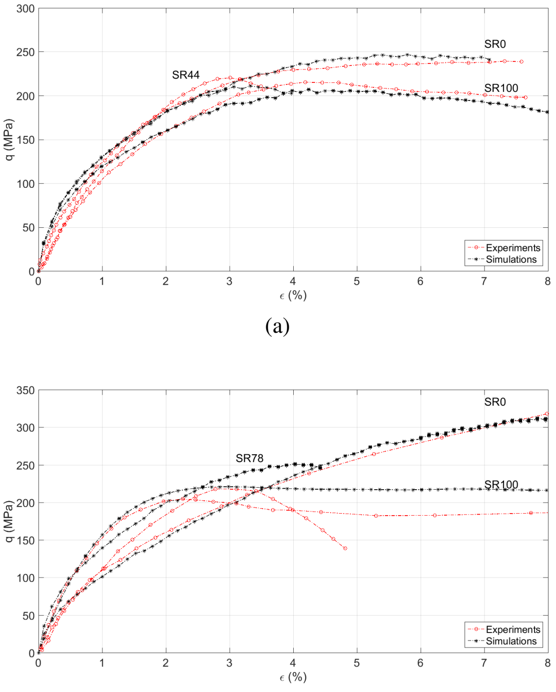

(a)

(b)

Fig. 14 Deviatoric phase of triaxial tests, deviatoric stress vs. axial strain for different saturation ratios ($S_r = 0\%$, $S_r = 44\%$, $S_r = 78\%$ and $S_r = 100\%$): comparison between experiment and modelling. a 100 MPa confinement. b 200 MPa of confinement

4.3.3 Oedometric tests

The static quasi oedometric compression (QOC) test allows testing the mechanical response of the material under a quasi-uniaxial strain loading path while applying a passive confinement. The difference between hydrostatic and quasi oedometric tests lies mainly in the volumetric strains reached for the same mean stress. During this test, a cylindrical specimen, tightly enclosed in a confinement vessel, is axially compressed by means of high strength compression plugs as stated by [3]. To simulate the quasi oedometric test, the sample is placed between six rigid walls. The axial displacement of both top and bottom walls are controlled while blocking all four other walls to simulate a uniaxial confined compression test under uniaxial strain. Figure 15 shows predictive mean stress evolution obtained for different saturation ratios. An experimental result obtained on a dry sample is also shown. The behavior of the numerical sample for $S_r = 0\%$ is very close to the experimental behavior. The effect of free water is also shown by means of numerical simulations. As expected, the results reveal that when the sample saturation increases, its oedometric stiffness also increases.

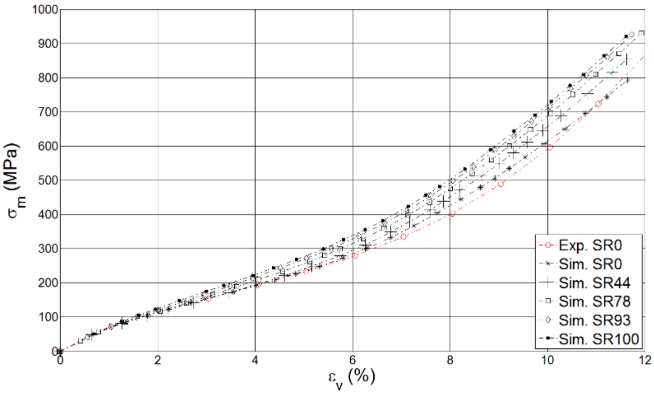

Fig. 15 Simulation of oedometric compression tests: mean stress vs. volumetric strain for different saturation ratios (Experiment Sr=0%; Numerical simulation $S_r = 0\%$, $S_r = 44\%$, $S_r = 78\%$ and $S_r = 100\%$)

5 Conclusion

The DE model presented in this paper is dedicated to the modelling of concrete behavior at very high stress level. To take into account the influence of free water during porosity closure that is observed in experiments, a new behavior law was developed at the scale of links between DEs. This constitutive behavior is based on a dependency of inelastic deformations of concrete and maximum shear stress criterion with the saturation ratio. The results show that the model is able to well reproduce the behavior of concrete samples on a wide range of stress levels (triaxial compression with a confining pressure up to 600 MPa) and on a wide range of saturation ratios ($S_r = 0$ to 100%). The identification of parameters is carried out thanks to tests performed on dry samples. The simulation results obtained for various loading paths and saturation ratios demonstrate the efficiency of the approach to take into account the influence of free water at very high stress level. As a perspective, simulations at a larger scale on concrete structures are feasible and will allow the evaluation of saturation ratio effects at a structural scale. The effect of saturation ratio on the behavior of concrete structures submitted to penetration or perforation tests will be evaluated thanks to this model.

Acknowledgements This research were financially supported by CEA DAM, the Direction of military applications of the French Alternative Energies and Atomic Energy Commission. The authors would also like to thank Dr. Christophe Pontiroli for scientific advice.

Conflict of interest

The authors declare that they have no conflict of interest.

References

1. Accary A, Malecot Y, Daudeville L (2019) Design and evaluation of a deformable sensor for interstitial pore pressure measurement in concrete under very high stress level. Applied Sciences 9(13):2610
2. Benniou H (2016) Modélisation par éléments discrets du comportement des matériaux ci- mentaires sous impact sévère prise en compte du taux de saturation. Ph.D. Dissertation, Grenoble Alpes University, France
3. Burlion N, Pijaudier-Cabot G, Dahan N (2001) Experimental analysis of compaction of concrete and mortar. International Journal for Numerical and Analytical Methods in Geomechanics 25(15):1467–1486
4. Cundall P, Strack ODL (1979) A discrete numerical model for granular assemblies. Geotechnique 29(1):47–65
5. Cusatis G, Pelessone D, Mencarelli A (2011a) Lattice Discrete Particle Model (LDPM) for failure behavior of concrete. I: Theory. Cement and Concrete Composites 33(9):881–890
6. Cusatis G, Mencarelli A, Pelessone D, Baylot J (2011b) Lattice Discrete Particle Model (LDPM) for failure behavior of concrete. II: Calibration and validation. Cement and Concrete Composites 33(9): 891–905
7. Daudeville L, Malecot Y (2011) Concrete structures under impact. European Journal of Environmental and Civil Engineering 15(sup1):101–140
8. Davis RO (1972) Thermodynamic response of Mie-Grüneisen materials at high pressures. Physik der kondensierten Materie 15(3):230–236
9. Donze F, Magnier S, Daudeville L, Mariotti C, Davenne L (1999) Numerical study of compressive behavior of concrete at high strain rates. ASCE Journal of Engineering Mechanics 125(10):31154–1163.
10. Frangin E, Marin P, Daudeville L (2006) On the use of combined finite/discrete element method for impacted concrete structures. Journal de Physique IV (Proceedings) 134:461–466
11. Gabet T (2006) Comportement triaxial du béton sous fortes contraintes: Influence du trajet de chargement. Ph.D. Dissertation, Grenoble Alpes University, France
12. Gabet T, Malecot Y, Daudeville L (2008) Triaxial behavior of concrete under high stresses: Influence of the loading path on compaction and limit states. Cement and Concrete Research 38(3):403–412
13. Gran JK, Frew DJ (1997) In-target radial stress measurements from penetration experiments into concrete by ogive-nose steel projects. International Journal of Impact Engineering 19:715–726
14. Hentz S, Donze F, Daudeville L (2004) Identification and Validation of a Discrete Element Model for Concrete. ASCE Journal of Engineering Mechanics 130(6):709–719
15. Kozicki J, Donze F (2009) YADE OPEN DEM: an open source software using a discrete element method to simulate granular material. Engineering Computations 26(7):786–805
16. Kozicki J, Tejchman J, Műhlhaus HB (2014) Discrete simulations of a triaxial compression test for sand by DEM. International Journal for Numerical and Analytical Methods in Geomechanic 38(18):1923–1952
17. Lilliu G, van Mier JGM (2003) 3D lattice type fracture model for concrete. Eng Fracture Mech 70:927–941
18. Malecot Y, Zingg L, Briffaut M, Baroth J (2019) Influence of free water on concrete triaxial behavior: The effect of porosity. Cement and Concrete Research 120:2017–216
19. Malecot, Y., Daudeville, L., Dupray, F., Poinard, C. and Buzaud, E. (2010), "Strength and damage of concrete under high triaxial loading", *European Journal of Environmental and Civil Engineering*, **14**(6-7), 777–803.
20. Mariotti C, Perlat JP, Guerin JM (2003) A numerical approach for partially saturated geomaterials under shock. International Journal of Impact Engineering 28(2):717–741
21. Nitka M, Tejchman J (2015) Modelling of concrete behaviour in uniaxial compression and tension with DEM. Granular Matter 17(1):145–164
22. Piotrowska E, Malecot Y, Ke Y (2014) Experimental investigation of the effect of coarse aggregate shape and composition on concrete triaxial behavior. Mechanics of Materials 79:45–57
23. Poinard C, Malecot Y, Daudeville L (2010) Damage of concrete in a very high stress state: Experimental investigation. Materials and Structures 43(1-2):15–29
24. Poinard C, Piotrowska E, Malecot Y, Daudeville L, Landis E (2012) Compression triaxial behavior of concrete: the role of the mesostructure by analysis of X-ray tomographic images. European Journal of Environmental and Civil Engineering 16(1):115–136
25. Pontiroli C, Rouquand A, Mazars J (2010) Prediction concrete behaviour from quasi-static loading to hypervelocity impact An overview of the PRM model. European Journal of Environmental and Civil Engineering 14(6-7):703–727
26. Potapov S, Masurel A, Marin P, Daudeville L (2017) Mixed DEM/FEM modeling of advanced damage in reinforced concrete structures. Journal of Engineering Mechanics 143(2):04016110
27. Potyondy D (2009) Stiffness matrix at a contact between two clumps. Itasca consulting Group, Inc., Minneapolis, MN
28. Rousseau J, Frangin E, Marin P, Daudeville L (2008) Damage prediction in the vicinity of an impact on a concrete structure: a combined FEM/DEM approach. Computers and Concrete 5(4):343–358
29. Rossi P., Van Mier J. G. M., Boulay C., Le Maou F. (1992) The dynamic behaviour of concrete: influence of free water. Materials and Structures 25(9): 509-514
30. Schlangen E, Garboczi E (1997) Fracture simulations of concrete using lattice models : Computational aspects. Engineering fracture mechanics 57(2/3):31–332
31. Shiu WJ, Donze F, Daudeville L (2008a) Penetration prediction of missiles with different nose shapes by the discrete element numerical approach. Computers and structures 86(21-22):2079–2086
32. Shiu WJ, Donze F, Daudeville L (2008b) Compaction process in concrete during missile impact: a DEM analysis. Computers and Concrete 5(4):329–342
33. Shiu WJ, Donze F, Daudeville L (2009) Influence of the reinforcement on penetration and perforation of concrete targets: a discrete element analysis. Engineering Computations 26(1-2):29–45
34. Smith J, Cusatis G (2016) Numerical analysis of projectile penetration and perforation of plain and fiber reinforced concrete slabs. International Journal for Numerical and Analytical Methods in Geomechanics 41(3):315–337

35. Suchorzewski J, Tejchman J, Nitka M (2018) Discrete element method simulations of fracture in concrete under uniaxial compression based on its real internal structure. International Journal of Damage Mechanics 27(4):453–487
36. Sun X, Wang H, Cheng X, Sheng Y (2020) Effect of pore liquid viscosity on the dynamic compressive properties of concrete. Construction and Building Materials 231, 117143.
37. Vu XH, Malecot Y, Daudeville L (2009a) Strain measurements on porous concrete samples for triaxial compression and extension tests under very high confinement. Journal of Strain Analysis for Engineering Design, 44(8):633–657
38. Vu XH, Malecot Y, Daudeville L, Buzaud E (2009b) Experimental analysis of concrete behavior under high confinement: effect of the saturation ratio. International Journal of Solids and Structures 46(5):1105–1120.
39. Vu XH, Malecot Y, Daudeville L (2011) Effect of coarse aggregate size and cement paste volume on concrete behavior under high triaxial compression loading. Construction and Building Materials 25(10):3941–3949
40. Vu XD, Malecot Y, Briffaut M, Daudeville L, Bertrand C (2015) Influence of the Saturation Ratio on Concrete Behavior under Triaxial Compressive Loading. Science and Technology of Nuclear Installations Article ID 976387
41. Wu S, Chen X, Zhou J (2012) Influence of strain rate and water content on mechanical behavior of dam concrete. Construction and Building Materials 36: 448-457.
42. Yankelevsky DZ, Dancygier AN (2001) Uniaxial compressive strength effect on high velocity penetration into thick NSC and HSC targets. Symposium ISIEMS
43. Yankelevsky DZ (1997) Local response of concrete slabs to low velocity missile impact. International Journal of Impact Engineering 19(4):331–343
44. Yip M, Li Z, Liao BS, Bolander JE (2003) Irregular lattice models of fracture of multiphase particulate materials. Int J Fracture 140:113–124
45. Zhou J, Chen X, Wu L, Kan X (2011) Influence of free water content on the compressive mechanical behaviour of cement mortar under high strain rate. Sadhana, 36(3), 357.
46. Zingg L, Briffaut M, Baroth J, Malecot Y (2016) Influence of cement matrix porosity on the triaxial behaviour of concrete. Cement and Concrete Research 80:52–59